Optics Letters

Fast quantum ghost imaging with a single-photon-sensitive time-stamping camera

Alex Mavian,[1,*] Yang Xu,[2] Cheng Li,[3] and Robert W. Boyd[2,3,4]

[1]Department of Physics, Applied Physics, and Astronomy, Rensselaer Polytechnic Institute, Troy, New York 12180, USA
[2]Department of Physics and Astronomy, University of Rochester, Rochester, New York 14627, USA
[3]Department of Physics, University of Ottawa, Ottawa, Ontario K1N 6N5, Canada
[4]The Institute of Optics, University of Rochester, Rochester, New York 14627, USA
*maviaa@rpi.edu

Received 21 October 2024; revised 11 December 2024; accepted 16 December 2024; posted 16 December 2024; published 13 January 2025

Quantum ghost imaging (QGI) leverages correlations between entangled photon pairs to reconstruct an image using light that has never physically interacted with an object. Despite extensive research interest, this technique has long been hindered by slow acquisition speeds, due to the use of raster-scanned detectors or the slow response of intensified cameras. Here, we utilize a single-photon-sensitive time-stamping camera to perform QGI at ultra-low-light levels with rapid data acquisition and processing times, achieving high-resolution and high-contrast images in under 1 min. Our work addresses the trade-off between image quality, optical power, data acquisition time, and data processing time in QGI, paving the way for practical applications in biomedical and quantum-secured imaging.

https://doi.org/10.1364/OL.544786

Introduction. In ghost imaging systems, two correlated fields are spatially separated into two independent paths [1]. One field illuminates an object and is captured by a bucket (single-pixel) detector, while the other field is imaged onto a spatially resolving detector [2]. Individually, neither detector provides the information necessary to produce an image, but the object can be revealed in the coincidence counts between the two detectors [3]. Ghost imaging was first observed by Pittman *et al.* in 1995 [4,5] by using entangled photons generated through spontaneous parametric downconversion (SPDC). In this nonlinear interaction, a single incoming pump photon is annihilated to create a pair of signal and idler photons, which can exhibit strong correlations in position and strong anticorrelations in transverse momentum [6,7]. These types of correlations, which can be used to demonstrate the Einstein–Podolsky–Rosen (EPR) paradox, allow the formation of a sharp and high-contrast image of the object [8–10]. While many of the initial imaging results were later similarly reproduced using spatially correlated classical light sources (thermal and pseudothermal) [11–14], quantum ghost imaging (QGI) remains advantageous in low-light conditions [15], offering a higher signal-to-noise ratio (SNR) and better visibility compared to approaches using classical sources [2,16]. The low-photon flux, combined with the robustness against scattering [17,18], makes QGI particularly well-suited for imaging photosensitive biological samples [19]. Additionally, nondegenerate photon pairs can be produced, allowing the object to be probed with one wavelength while capturing its spatial information at a different wavelength [20,21]. This approach may be used to overcome limitations in the spectral bandwidth of a detector and assist in covert operations [22,23].

A key objective in QGI is to achieve the highest resolution and contrast within the shortest acquisition time, ideally surpassing the capabilities of classical methods [16]. However, due to the lack of single-photon-sensitive fast cameras [24], early experiments relied on raster scanning point-like detectors to simulate a camera [1,4]. This approach sets a maximum detection efficiency to $1/N$, where N is the number of scanned pixels [8]. The use of time-gated intensified charge-coupled device (ICCD) cameras for spatial detection marked a significant improvement, allowing detection efficiency to linearly scale with the number of pixels, N, in the image [8]. In this scheme, time-correlation measurements are conducted by triggering the ICCD when the bucket detector registers a signal. However, compensating for the slow gating electronics of the ICCD requires a 20–30 m long image-preserving delay line, adding complexity to practical implementation. Moreover, because the average number of photon events per pixel must remain well below one and the ICCD frame rate is limited to the kHz range (due to data output constraints [25]), data acquisition time often spans hours. Another advancement occurred with the development of single-photon avalanche diode (SPAD) arrays, offering single-photon detection with high temporal resolution, albeit typically at a lower transverse resolution (~1000 pixels) [26]. In 2023, Gili *et al.* used a 2D SPAD array technology to demonstrate QGI [27] on the time scale of minutes, although the imaging suffered from low spatial resolution (32×32 pixels) and substantial noise at sub-minute acquisition times. In 2024, Davenport *et al.* used a pair of time-synchronized SPAD arrays to achieve high-SNR ghost images and enhanced contrast within seconds [28].

In this work, we employ a single-photon-sensitive time-stamping camera (Tpx3Cam) to overcome the limitations on the spatial and temporal resolution of QGI in the low-photon regime. The Tpx3Cam camera (Amsterdam Scientific Instruments), in combination with an image intensifier (Photonis),

time-tags the arrival of individual photons. The camera features a 256×256 silicon pixel array, with a pixel size of 55×55 μm and a temporal resolution of 1.56 ns, supporting a maximum output rate of 80 Mpix/s [25]. When operating between the wavelengths of 600 and 850 nm, the Hi-QE Red photocathode in the image intensifier offers a quantum efficiency (QE) of approximately 20%, with the entire system at an efficiency of $7.4 \pm 2\%$ [24]. Unlike traditional CCD or CMOS cameras, which capture signals frame by frame, the Tpx3Cam operates in an entirely data-driven manner, recording the timestamped information for each pixel [25]. This approach enables continuous fast readout and offers flexibility in complex analyses, such as spatially resolved time-coincidence measurements. The Tpx3Cam is exceptionally well-suited for quantum imaging experiments and has already been applied to snapshot hyperspectral imaging [29], polarization entanglement characterization [30], quantum light-field microscopy [31], and studies of spectral–temporal correlations in the Hong–Ou–Mandel interference [32].

Experiment. The setup is illustrated in Fig. 1(a). A continuous-wave (CW) 405 nm laser with an output of 2 mW is used to pump a beta-barium borate (β-BBO) crystal, phase-matched for type-II degenerate SPDC, to produce entangled photon pairs at around 810 nm. The pump laser is linearly polarized, tuned with a half-wave plate (HWP) to maximize SPDC conversion efficiency, and spatially filtered to isolate a single mode. The down-converted photons, produced in orthogonal polarizations, are split into two paths using a polarizing beam splitter (PBS). We denote the reflected photons as *signal* and the transmitted photons as *idler*. The signal photons are first imaged onto the object using a 2-f system and then imaged onto the camera through free-space propagation, while the idler photons are directly imaged onto the camera using another 2-f system with a different focal length. The paths of the signal and idler beams are then made collinear using a second PBS and are incident on different areas of the camera sensor. A 715 nm longpass filter (LPF) is placed immediately after the nonlinear crystal to block the pump beam, while two 810/3 nm bandpass filters (BPFs) in front of the camera reject stray light from the pump beam and background illumination.

Post-processing is performed in PixGUI [33], a program designed for processing, viewing, and analyzing quantum imaging data from the Tpx3Cam. In the GUI, a virtual rectangular aperture is applied around each beam to confine the region for time-coincidence analysis. Consequently, the Tpx3Cam sensor is digitally partitioned to function as both a bucket detector for the signal beam and a spatially resolving detector for the idler beam, as was recently demonstrated with a SPAD array [34]. A centroiding algorithm is then employed to detect single-photon events within the clusters of pixels illuminated by the image intensifier [25]. For each of these events, the correct time of arrival (TOA) and time over threshold (TOT) are calculated and added to an array of events. The array is subsequently filtered using a pairing algorithm that considers only photon pairs detected within a 10 ns time window. While the processing time largely depends on the available computational resources, in our case (Intel i9-13900, 3 GHz, 24-core CPU, and 32 GB memory), data processing with PixGUI takes approximately 1 min for a 30 s acquisition. Because the positions of photons are anticorrelated in the far field of the crystal, the ghost image is inverted with respect to the object in our setup [1]. In this Letter, the images have been digitally re-inverted without any additional processing. Unless otherwise

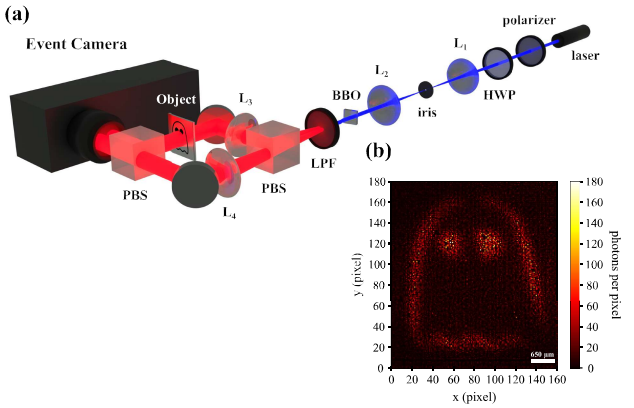

Fig. 1. (a) Experimental setup of QGI utilizing the momentum correlations in the entangled photon source. L_1 and L_2 are anti-reflection-coated lenses with focal lengths of 75 cm. L_3 = 10 cm and L_4 = 15 cm. The two 810/3 nm BPFs directly on the camera are not pictured here. (b) Ghost image of a ghost-shaped object from a total of 51,901 coincidences captured over 150 s.

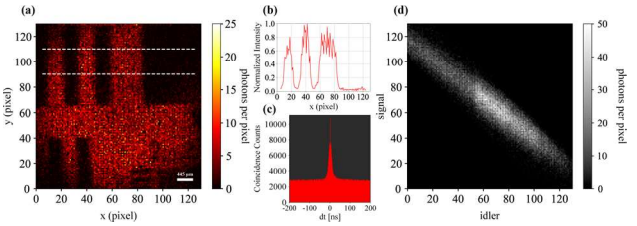

Fig. 2. (a) Ghost image of a section of the USAF resolution test chart from a total of 47,004 coincidences. (b) Cross section of the image averaged over the 20 rows indicated by the dashed lines. (c) Coincidence peak representing photon pairs. (d) JPD demonstrating anticorrelation in transverse momentum.

specified, the data acquisition time for the images presented in this Letter is 30 s. Such an integration time was selected to present high-SNR images, although shorter acquisition times of just a few seconds could still adequately capture the object's features.

Results. In Fig. 2, we demonstrate the ghost imaging capabilities of the Tpx3Cam. Using a 1951 United States Air Force (USAF) resolution test chart, we achieve a high-contrast ghost image with a resolution of 130×130 pixels (Fig. 2(a)) and resolve the 111.36 μm linewidth of element 2. This resolution is limited by the point-spread function of the system [35] and could be further enhanced with better optical components, such as a microscope objective. A normalized cross section of the ghost image (Fig. 2(b)) depicts high image contrast, which we calculate to be 89% using the following equation:

$$C = \frac{I_{max} - I_{min}}{I_{max} + I_{min}}, \tag{1}$$

where $I_{\max}$ is the average maximum intensity of the signal and $I_{\min}$ is the corresponding average minimum intensity from the adjacent region where the signal drops due to the object obscuring the light. The coincidence histogram (Fig. 2(c)) clearly shows a peak corresponding to photon pairs with similar TOA, with a coincidence-to-accidental ratio of ~3.8 and a FWHM of 6 ns. In Fig. 2(d), we present the joint probability distribution (JPD), which displays anticorrelations in the transverse momentum of

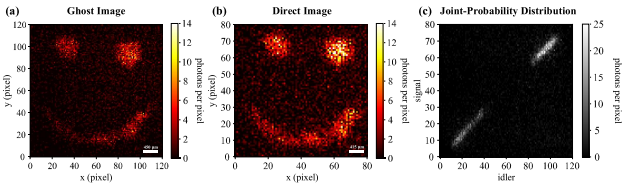

Fig. 3. (a) Ghost image of a smiley face from a total of 8383 coincidences and (b) the corresponding temporally filtered direct image. (c) JPD demonstrating positive correlations.

the down-converted photons. If the object and imaging detector were placed in a near-field configuration, the JPD would exhibit a positive correlation, showing the correlation in the transverse position of the down-converted photons.

One of the advantages of the Tpx3Cam system is its ability to simultaneously capture both a ghost image from the idler photons in the coincidence pairs and a direct image from the signal photons in the coincidence pairs. This scheme can allow imaging of different transverse planes of an object, enabling light-field microscopy [31] or phase imaging [36]. By placing a short focal length lens after the object ($f = 2.5$ cm), the spatial information from the illuminated object is imaged onto the event camera, preventing it from being lost to diffraction. In this setup, the pixels detecting signal photons continue to function as the bucket detector and do not affect the ghost image, but now a temporally filtered direct image is also formed. The distinction between the direct and ghost image is determined by whether the spatial information is obtained from the signal or the idler photons, respectively. One benefit of the ghost image is that it can be configured to be more resilient to turbulence or scattering [17,18]. In Fig. 3, we present a ghost image of a smiley face alongside the corresponding direct image. The difference in resolution between the two images arises from the signal and idler beams being magnified by different amounts, leading them to occupy areas of different sizes on the camera sensor. We also show the JPD (Fig. 3(c)), which now displays a positive correlation due to the imaging lens inverting the position information from the object.

According to the quantum imaging theory [37], the SNR of an image scales with the square root of the integration time. Here, we illustrate the improvement of image quality with increasing data acquisition time using the Tpx3Cam. In Figs. 4(a)–4(d), we present four ghost images with various acquisition times. In Fig. 4(e), we plot SNR in variance with the acquisition time [27], showing good agreement with the theory. In order to calculate the SNR, we use the following equation:

$$SNR = \frac{I_{signal}}{\sigma_{bg}}, \tag{2}$$

where I_{signal} represents the signal intensity and σ_{bg} is the standard deviation of the background. In this case, because the object blocks the beam instead of transmitting photons, the surrounding illuminated area is treated as the signal, while the object itself, which obstructs the light, is considered the background. Using this method, we calculate an SNR of 12 for the image in Fig. 2. Although these images exhibit strong contrast, the substantial pixel-to-pixel variation—stemming from the Poissonian statistics of shot noise—limits the SNR [38]. One approach to improve image quality while remaining in the low-photon regime is to apply reconstruction techniques that optimize the

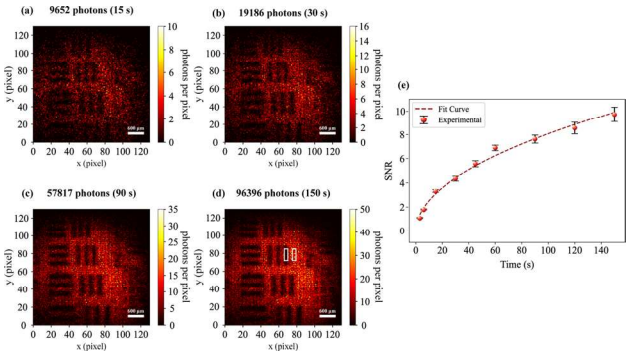

Fig. 4. Ghost images of USAF resolution chart integrating over (a) 15 s, (b) 30 s, (c) 90 s, and (d) 150 s. (e) Plot of SNR of ghost images against data acquisition time with theoretical fit. The signal intensity and background noise are measured in the rectangular regions displayed in (d).

sparsity of the contributing spatial frequencies, similar to the method used in JPEG image compression [15,39]. Nonetheless, even without these techniques, the object features are still visible with low-photon numbers (less than 10 per pixel and an average of 0.58 photons for Fig. 4(a)).

Discussion. In this work, we have successfully demonstrated a fast QGI system using a single-photon-sensitive time-stamping camera, capable of producing high-contrast and high-resolution images with ultra-low-light levels (on the order of 10^5 total photons). While related quantum imaging techniques have been explored using event cameras [29,31,40,41], to our knowledge, this is the first instance of QGI with these specific capabilities. With a 30 s acquisition time and 2 mW pump power, we achieved QGI with ~90% contrast and an SNR of 12 for the data shown in Fig. 2. For comparison, the recent study using dual SPAD detectors reported ~25% contrast and an SNR of 40 at a 10 s acquisition time with 11 mW of pump power [28]. Furthermore, the Tpx3Cam's 256×256 pixel array provides significantly higher resolution images compared to the 32×32 SPAD array. While a direct comparison is difficult, it is clear that the Tpx3Cam outperforms the SPAD in terms of contrast and spatial resolution under these experimental conditions. In addition to the higher temporal resolution of the SPAD (50 ps), the larger SNR can be partially attributed to the higher flux of down-converted photons from a greater pump power. Interestingly, a recent work with the Tpx3Cam uses spatial filtering methods to overcome accidental coincidences, achieving sub-second quantum-correlated imaging through noisy channels [42].

Although this progress brings us closer to the goal of real-time quantum imaging, further technical improvements in cameras will be required to make quantum imaging technology a reality. As we observed, the SNR scales with the square root of the integration time due to the greater amount of data being acquired. Similarly, the SNR increases with the square root of the timing resolution. While the Tpx3Cam is designed with a temporal resolution of 1.56 ns, the effective timing resolution has been estimated at approximately 7.3 ns [24]. This is significant because faster time-tagging would reduce the chance of accidental coincidences and decrease the acquisition time needed to achieve the same image quality. Fortunately, with ongoing developments in Timepix [43] and SPAD array technologies [44], we can expect more practical demonstrations of QGI in the future.

Additionally, a recent study using a photocathode-based non-pixelated "Ncam" detector (0.5 ns timing resolution) achieved high-quality ghost images of binary targets within 1 min and ghost images of plant material within 40 min [45]. Although these results are impressive, Ncam can detect only one photon at a time, which leads to longer data acquisition times despite a higher pump power. In contrast, the Tpx3Cam has the added advantage of serving as both an image sensor and a bucket detector. This dual functionality allows for the simultaneous acquisition of images at two distinct planes, facilitating the collection of more complete information about the object. Such an approach could enable novel applications, including volumetric microscopy [31] or 3D ghost imaging, which has previously been demonstrated using asynchronous SPADs [46,47]. Furthermore, our setup offers the potential to incorporate techniques such as interaction-free measurement to achieve enhanced sensitivity with even fewer photons [48,49]. Additionally, the integration of machine learning methods such as those used in computational ghost imaging [16,50] could further reduce data acquisition time and mitigate the effects of shot noise. We believe that these combined advancements will make quantum ghost imaging a viable tool for real-world applications beyond the laboratory.

Funding. National Science Foundation (2244031); U.S. Department of Energy (76295); Natural Sciences and Engineering Research Council of Canada (RGPIN/2017-06880); Canada First Research Excellence Fund (072623).

Acknowledgment. We thank Brayden Freitas for helpful advice on using PixGUI for data processing and Andrei Nomerotski for insightful discussions regarding the Tpx3Cam camera.

Disclosures. The authors declare no conflicts of interest.

Data availability. Data underlying the results presented in this Letter are not publicly available at this time but may be obtained from the authors upon reasonable request.

REFERENCES

1. M. J. Padgett and R. W. Boyd, Phil. Trans. R. Soc. A **375**, 20160233 (2017).
2. B. I. Erkmen and J. H. Shapiro, Adv. Opt. Photonics **2**, 405 (2010).
3. J. H. Shapiro and R. W. Boyd, Quantum Inf Process **11**, 949 (2012).
4. T. B. Pittman, Y. H. Shih, D. V. Strekalov, *et al.*, Phys. Rev. A **52**, R3429 (1995).
5. D. V. Strekalov, A. V. Sergienko, D. N. Klyshko, *et al.*, Phys. Rev. Lett. **74**, 3600 (1995).
6. W. Zhang, R. Fickler, E. Giese, *et al.*, Opt. Express **27**, 20745 (2019).
7. B. Courme, C. Vernière, P. Svihra, *et al.*, Opt. Lett. **48**, 3439 (2023).
8. R. S. Aspden, D. S. Tasca, R. W. Boyd, *et al.*, New J. Phys. **15**, 073032 (2013).
9. J. C. Howell, R. S. Bennink, S. J. Bentley, *et al.*, Phys. Rev. Lett. **92**, 210403 (2004).
10. A. Saxena, M. Kaur, V. Devrari, *et al.*, Sci. Rep. **12**, 21105 (2022).
11. R. S. Bennink, S. J. Bentley, R. W. Boyd, *et al.*, Phys. Rev. Lett. **92**, 033601 (2004).
12. F. Ferri, D. Magatti, A. Gatti, *et al.*, Phys. Rev. Lett. **94**, 183602 (2005).
13. A. Valencia, G. Scarcelli, M. D'Angelo, *et al.*, Phys. Rev. Lett. **94**, 063601 (2005).
14. A. Gatti, M. Bache, D. Magatti, *et al.*, J. Mod. Opt. **53**, 1 (2006).
15. P. A. Morris, R. S. Aspden, J. E. C. Bell, *et al.*, Nat. Commun. **6**, 5913 (2015).
16. C. Moodley and A. Forbes, Sci. Rep. **12**, 10346 (2022).
17. Y.-K. Xu, W.-T. Liu, E.-F. Zhang, *et al.*, Opt. Express **23**, 32993 (2015).
18. P. B. Dixon, G. A. Howland, K. W. C. Chan, *et al.*, Phys. Rev. A **83**, 051803 (2011).
19. R. Weissleder, Nat. Biotechnol. **19**, 316 (2001).
20. K. W. C. Chan, M. N. O'Sullivan, and R. W. Boyd, Phys. Rev. A **79**, 033808 (2009).
21. R. S. Aspden, N. R. Gemmell, P. A. Morris, *et al.*, Optica **2**, 1049 (2015).
22. X. Yao, X. Liu, L. You, *et al.*, Phys. Rev. A **98**, 063816 (2018).
23. Y. Xu, S. Tang, A. N. Black, *et al.*, Opt. Express **31**, 42723 (2023).
24. V. Vidyapin, Y. Zhang, D. England, *et al.*, Sci. Rep. **13**, 1009 (2023).
25. A. Nomerotski, Nucl. Instrum. Methods Phys. Res., Sect. A **937**, 26 (2019).
26. H. Defienne, P. Cameron, B. Ndagano, *et al.*, Nat. Commun. **13**, 3566 (2022).
27. V. F. Gili, D. Dupish, A. Vega, *et al.*, Appl. Opt. **62**, 3093 (2023).
28. D. Davenport, A. Eshun, B. Demory, *et al.*, Opt. Express **32**, 36031 (2024).
29. Y. Zhang, D. England, and B. Sussman, Opt. Express **31**, 2282 (2023).
30. C. Ianzano, P. Svihra, M. Flament, *et al.*, Sci. Rep. **10**, 6181 (2020).
31. Y. Zhang, D. England, A. Orth, *et al.*, Phys. Rev. Appl. **21**, 024029 (2024).
32. Y. Zhang, D. England, A. Nomerotski, *et al.*, Opt. Express **29**, 28217 (2021).
33. B. Freitas, "PixGUI," GitHub (2024), https://github.com/baf57/PixGUI.
34. V. S. Starovoitov, V. N. Chizhevsky, D. Mogilevtsev, *et al.*, Appl. Opt. **63**, 6012 (2024).
35. P.-A. Moreau, E. Toninelli, P. A. Morris, *et al.*, Opt. Express **26**, 7528 (2018).
36. H. Hodgson, Y. Zhang, D. England, *et al.*, Appl. Phys. Lett. **122**, 034001 (2023).
37. A. Meda, E. Losero, N. Samantaray, *et al.*, J. Opt. **19**, 094002 (2017).
38. G. M. Morris, Appl. Opt. **23**, 3152 (1984).
39. E. J. Candes and M. B. Wakin, IEEE Signal Process. Mag. **25**, 21 (2008).
40. P. Svihra, Y. Zhang, P. Hockett, *et al.*, Appl. Phys. Lett. **117**, 044001 (2020).
41. Y. Zhang, A. Orth, D. England, *et al.*, Phys. Rev. A **105**, L011701 (2022).
42. B. Freitas, Y. Zhang, D. England, *et al.*, "Quantum correlated image recording through noisy and turbulent channels," Optica Open (2024).
43. X. Llopart, J. Alozy, R. Ballabriga, *et al.*, J. Instrum. **17**, C01044 (2022).
44. K. Morimoto, J. Iwata, M. Shinohara, *et al.*, in *2021 IEEE International Electron Devices Meeting (IEDM)* (IEEE Publishing, 2021), pp. 20.2.1–20.2.4.
45. D. P. Ryan, K. Meier, K. Seitz, *et al.*, Optica **11**, 1261 (2024).
46. C. Pitsch, D. Walter, L. Gasparini, *et al.*, Appl. Opt. **62**, 6275 (2023).
47. C. Pitsch, D. Walter, S. Grosse, *et al.*, Appl. Opt. **60**, F66 (2021).
48. Y. Zhang, A. Sit, F. Bouchard, *et al.*, Opt. Express **27**, 2212 (2019).
49. S. Ahmadi, E. Saglamyurek, S. Barzanjeh, *et al.*, Phys. Rev. A **107**, 032611 (2023).
50. C. Moodley, B. Sephton, V. Rodríguez-Fajardo, *et al.*, Sci. Rep. **11**, 8561 (2021).